PAPER • **OPEN ACCESS**

Topology optimization of 3D-printed mycelium hydrogels

To cite this article: Winston Lindqwister *et al* 2026 *Biofabrication* **18** 035013

Biofabrication

OPEN ACCESS

RECEIVED
18 February 2026

REVISED
1 June 2026

ACCEPTED FOR PUBLICATION
4 June 2026

PUBLISHED
26 June 2026

PAPER

Topology optimization of 3D-printed mycelium hydrogels

Winston Lindqwister[1,*], **Mrinal Chaudhury**[1], **Sarah Schyck**[1], **Iuri Rocha**[2], **Kunal Masania**[1] and **Martin Lesueur**[2]

[1] Faculty of Aerospace Engineering, Technische Universiteit Delft, Delft, The Netherlands
[2] Faculty of Civil Engineering and Geosciences, Technische Universiteit Delft, Delft, The Netherlands
[*] Author to whom any correspondence should be addressed.

E-mail: wlindqwister@gmail.com

Keywords: mycelium, hydrogel, topology optimization, fungi materials, engineered living materials

Supplementary material for this article is available online

Abstract

As we move towards more sustainable and resilient materials, new opportunities for harnessing the next generation of biological materials will arise. Materials composed of living organisms have great potential in fulfilling this role as a self-healing, lightweight and sustainable structural material. Recent advances in 3D-printing using fungi-inoculated hydrogels opens the potential of additive manufacturing with fungi into optimized shapes. However, while this technique of 3D-printing fungi has great potential in a wide range of engineering applications, computational models do not yet exist to precisely engineer the strength of structures made from this material. Here we create a computational modeling scheme for 3D-printed mycelium structures, linking the growth of fungi to stiffness. We first model the growth of fungi through a diffusion model. We then convert the resultant density values into local stiffness, creating a computational representation of the varying elemental stiffness as a function of local mycelial density. We implement two Bayesian optimization-based topology optimization schemes to maximize the strength of cuboid 3D-printed structures while minimizing the input material cost. One maximizes the material specific stiffness while the other applies a constrained scheme for identifying a minimized mass for a target design stiffness. Both show a distinct tradeoff in print mass to stiffness, with results validated experimentally. These new insights provide important next steps in the effective harnessing of this class of emergent material, as well as its larger adoption for engineering applications.

1. Introduction

As we move toward building the cities and infrastructures of the future, the adoption of new paradigms for smart, adaptable, and environmentally conscious building materials is critical to addressing the pressing challenges of sustainability and resilience in modern society [1]. One particularly promising class of materials for this purpose is engineered living materials (ELMs); materials composed of living cells. These materials are especially compelling due to their inherent capabilities to self-propagate, regenerate, and dynamically adapt to their environment [2–5].

The functionality of ELMs spans from microscale cellular behaviors to macroscale structural responses, yielding materials that are not only innately responsive but also hierarchically organized [6]. This added dimension of functionality introduces a complex design landscape, wherein the behavior of materials can be tuned from the cellular level up to the macroscopic scale [7].

A compelling subclass within ELMs is those comprised of fungal cells. Fungal organisms form a branching network of hyphae that interweave into a mycelium structure which is a fibrous network that serves as the primary structural component of the fungal body [8, 9]. In recent years, mycelium-based materials have garnered significant interest due to their potential applications as a morphable structural material, in electrical conductivity and signaling, and with responsiveness to external stimuli [10–12].

However, to engineer and design fungi-based materials, precise additive manufacturing tools have emerged as a route for development, where a custom-designed substrate acts as a scaffold for living cells to grow out of, creating a composite structure composed

of substrate and mycelium. These tools allow for the creation of metamaterials whose internal architectures can now be voxel-specifically designed and spatially tuned. In the context of engineered living systems, this flexibility allows for unprecedented design freedom, extending to shape, porosity, and microstructural function [13]. With porosity stemming both from the ELM microstructure and the printed scaffold, those materials offer remarkable strength-to-weight properties and tunable porosity, enabling applications ranging from enhanced surface-area exchange to improved matrix adhesion or biofilm integration [14–17].

Gantenbein *et al* [18], developed *Ganoderma lucidum*–inoculated hydrogels that were 3D printed into lattice architectures to facilitate simultaneous colonization of the gel and bridging across air gaps. They demonstrated that nutrient concentration (via malt extract content) and hydrogel rheology modifiers strongly influence fungal exploration vs. exploitation balance, i.e. whether the mycelium spreads broadly or densifies local pathways. Their system relied on agar-based hydrogel matrices with rheological tuning to maintain printability, humidity control during incubation to support fungal growth, and open-architecture lattice designs that allow hyphae to traverse void spaces effectively. By combining these chemical and physical controls with geometric design, they produced living materials that self-repair, regenerate, and adapt to damage, serving as a direct experimental basis for the computational design framework developed here.

In this process, the printed hydrogel geometry defines the macroscopic scaffold, while the subsequent fungal colonization generates a secondary level of porosity at the microscale. This dual form of organization, with geometry imposed by printing and microstructure emerging from biological growth, naturally yields a hierarchical porous material. The resulting system couples physical design freedom with biologically driven variability, enabling tunable performance from the perspective of the macroscale that directly impacts the microstructure development of the material. This approach enables first-of-its-kind control over the geometry of fungal structures, opening doors to a wide range of engineering applications such as functional living skins for robots, graded porosity in composites, and bio-signaling pathways embedded in fungal networks [19–21]. Leveraging the geometric and topological freedom of 3D printing, fungal structures can be shaped into diverse patterns and forms tailored to their intended functionalities.

Despite the promise of this technique, a key limitation remains, which is the prediction of shape and performance for a given living hydrogel structure. While models do exist for predicting the growth and saturation of fungal networks, they do not directly translate fungal growth into a metric of material performance [22–24]. At present, 3D printing of fungal materials remains at a proof-of-concept stage. While early demonstrations highlight their potential for lightweight and sustainable structures, the absence of a robust parametric understanding of fungal behavior prevents effective optimization. This limitation arises primarily from the coupling between biological growth dynamics and print geometry, which are difficult to quantify within a unified design framework. This gap hinders the efficient design of structural forms, particularly when strength-to-weight ratio is a critical consideration. Efficient material use is a fundamental goal in additive manufacturing, especially when sustainability and minimal environmental impact are central concerns [25, 26].

Further complicating the design challenge is the structure of the fungi-inoculated hydrogel. While the hydrogel matrix constitutes the bulk of the material's mass, the mycelium network functions as the primary load-bearing component. Thus, the primary design technique for this method is inherently indirect, as the relevant structure is grown from the printed component. Furthermore, the interplay between the engineered hydrogel scaffold and the biologically grown mycelial network is key in applications requiring high stiffness at low mass where optimizing material distribution for high properties at low weight is paramount [27, 28].

To address this indirect coupling between the designed and the grown components, topology optimization emerges as an essential framework for exploring structural efficiency within biologically based materials. Traditional topology optimization approaches such as variable-density formulations and the solid isotropic material with penalization technique can produce highly intricate architectures across a broad design space suitable for additive manufacturing. However, these continuous methods fail to incorporate microscale biological phenomena, such as fungal growth dynamics, and are computationally expensive due to their large number of degrees of freedom [29–32].

The structural optimization of hierarchical porous living materials therefore remains a largely unsolved problem. Their formation processes are not only time-dependent and condition-sensitive but also governed by coupled biological, chemical, and physical interactions. Microstructural evolution is influenced by factors such as ink rheology, particle interactions, and nutrient gradients, resulting in morphologies that are difficult to parametrize or predict within standard optimization frameworks. Consequently, defining geometric descriptors suitable for continuous optimization is challenging, and high-fidelity

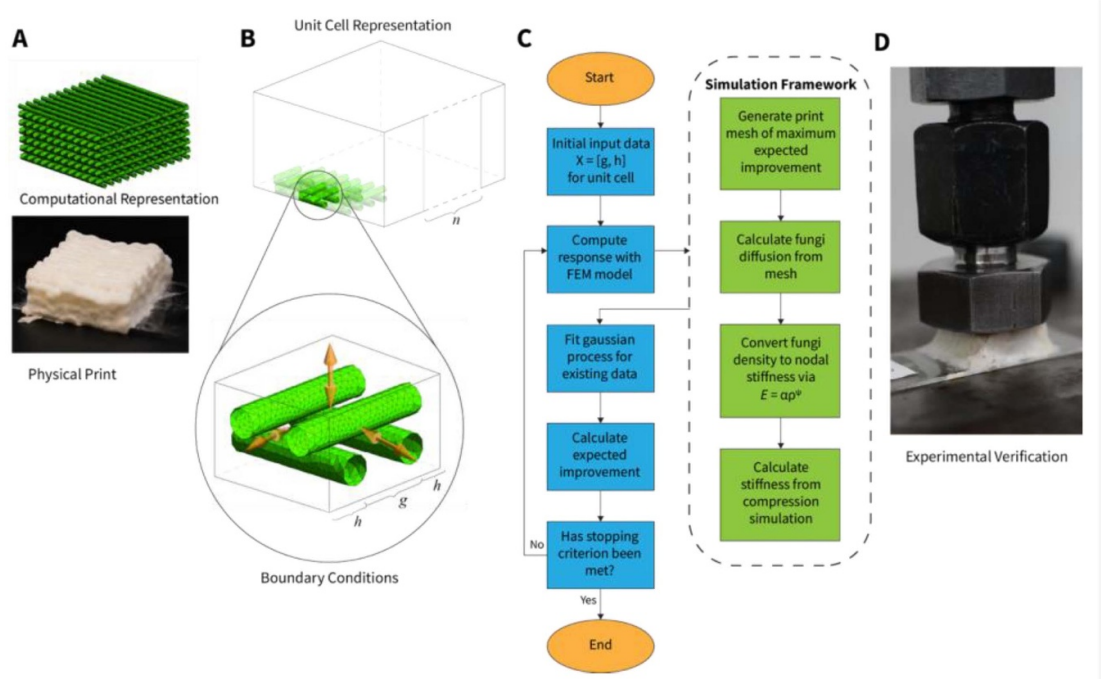

Figure 1. (A) Comparison of the computational representation of a mycelium hydrogel print to a physical print. (B) Illustration of the unit cell scheme for the prints, with periodic boundary conditions on the unit cell. (C) The general computational framework of this study, with a Bayesian optimization scheme linked to a generalized simulation framework. For our Bayesian optimization pipeline, a stopping criterion is triggered if the calculated specific stiffness γ does not improve by 0.5% over the last 50 iterations. A hard stopping criterion is also implemented after 1000 iterations. (D) Experimental set up for verifying compression values.

simulations often demand multiscale nonlinear finite element (FE) analyses that are computationally intensive and reliant on high-performance computing resources.

Parametric design models provide a natural bridge between the stochastic nature of biological growth and the deterministic frameworks of topology optimization. By simplifying the design space into a limited set of physically interpretable parameters for unit cells, an approach common for the design of periodic metamaterials, computational costs are drastically reduced while maintaining relevance to fabrication constraints [33]. Bayesian optimization has proven successful in efficiently navigating complex, low-dimensional design spaces such as those found in hyperparameter tuning and parametric structural optimization. However, its potential to optimize biologically driven geometries such as the print spacing of 3D-printed fungal hydrogels has not yet been realized due to its reliance on explicit parametrization [34]. This gap highlights a critical opportunity: to develop an optimization framework that couples biological growth models with parametric topology optimization, thereby enabling the systematic design of lightweight, living materials.

We introduce a computational framework that couples fungal growth modeling with parametric topology optimization to address this challenge. Specifically, we developed a model that captures the growth dynamics and mechanical performance of 3D-printed mycelium hydrogels, allowing the integration of biological processes into an engineering optimization pipeline. We implement a Bayesian optimization scheme to identify optimal print-spacing topologies within a constrained, physically interpretable design space. This approach bridges the gap between biology-driven material formation and computational structural optimization, advancing both the theoretical and practical toolkit for designing hierarchical ELMs.

2. Computational design

The goal of this project is to optimize the print topology of a 3D-printed fungal hydrogel and the resulting mycelial network with respect to performance under uniaxial compression, as illustrated in figures 1(A) and (B). The structures are printed as cuboids composed of filamentary hydrogel strands arranged in a lattice pattern, which allows the printed layers to stack directly on top of one another while maintaining mechanical stability and consistent layer adhesion during printing and incubation. This configuration ensures that each successive layer is physically supported by the one beneath it, preventing collapse or deformation of the hydrogel during fabrication and early growth.

Compared to a uniformly distributed filament design, the lattice arrangement also enables controlled variation in the spacing between filaments, a key parameter influencing both fungal colonization and local stiffness. By varying this spacing, we can tune the degree of porosity and the overall load-bearing performance of the resulting mycelial network. Due to the regularity of loading and geometric symmetry of these cuboids, the optimization problem can therefore be reduced to the study of a single periodic unit cell, as illustrated in figure 1(B). This strategy significantly alleviates the computational burden by constraining the design domain, allowing for faster iterative FE simulations and a more tractable search space for topology optimization.

The design of each unit cell is governed by two independent geometric parameters: g, the gap between the parallel hydrogel print lines, and h, the lateral overhang on both sides of each line. This parametrization enables a tunable degree of spacing heterogeneity where the special case of $h = \frac{g}{2}$ corresponds to uniformly spaced print lines. Meshes for the unit cell designs were created parametrically using the open source meshing software GMSH [35]. Opposite faces of the unit cells were assigned to be periodic nodes, and all elements were generated as Tet4 elements. The meshes were set to have a minimum element size of 0.01 mm and a maximum element size $\epsilon_{\max}$ relative to the thickness of the hydrogel filament δ ($\epsilon_{\max} = \min(0.3, \delta/2)$). Elements were refined along curvature points by 10 elements per 2p, with 0.1 mm of z-axis padding for nodal alignment along the top and bottom faces. FE simulations of uniaxial compression on the unit cell were run using the MOOSE framework [36] to reproduce the hyperelastic behaviour of the experimental mechanical tests, both from the literature and recreated in the lab. Mesh convergence reporting can be found in the supplementary material figure S4. For fabrication, these unit cells are tessellated evenly in 3D to generate full-scale printed cuboids for mechanical testing. This approach minimizes printing flaws by ensuring a regular, self-supporting lattice structure, while also providing samples of sufficient size for accurate compression testing. Moreover, the use of tessellated unit cells reflects the behavior of realistic metamaterials, which are typically composed of repeating periodic elements. It also reduces boundary effects that would otherwise dominate in small or isolated samples, as the periodic arrangement enables a more representative measurement of bulk material properties.

2.1. Modeling the material behavior of mycelial hydrogels

Confocal imaging data, visible in figures 2(A) and (B), and dry biomass data from previously published experimental work [18], visible in figure 2(C) were used to characterize and calibrate both the growth model of the mycelium as well as the three parameter Yeoh hyperelastic model for material stiffness. In this previous study, grayscale intensities from confocal images of fungi mycelium growing between two hydrogels were quantified over a five-day growth period and interpreted as indicators for fungal biomass accumulation. By looking at this data, we can qualitatively characterize the function used for mycelial growth, starting with a comparison of a 1D case and extrapolating to 3D. At the cellular scale, fungal growth occurs through the extension of individual hyphae; however, these hyphae rapidly aggregate into larger mycelial sheets that form the macroscale material. In an environment of constant nutrient concentration, this expansion proceeds as a diffusive front originating from the hydrogel filaments and propagates outward through the surrounding void space [37]. As established in mathematical biology literature, while discrete models are required to resolve cellular-level branching and anastomosis, the aggregate dynamics of mycelial network expansion at the colony scale are effectively captured using continuum reaction-diffusion frameworks [38]. As the front advances, adjacent growth regions merge, bridging the gaps between printed lines and effectively cementing the overall structure. Growth continues until the fungus either occupies the available voids or reaches its natural limit due to distance from the nutrient source (the hydrogel surface).

Given this behavior, the bulk evolution of the material can be sufficiently captured by modeling fungal growth as a diffusive process. Accordingly, the growth profile was represented computationally using a constant-coefficient diffusion equation to describe the net spread of mycelial biomass from the hydrogel boundary into the uncolonized regions. While micromodels that resolve cellular-level branching and chemotaxis can offer greater precision, the aggregate dynamics of mycelial expansion are effectively diffusive at the mesoscale and are thus well represented by this simplified formulation. Furthermore, the approach of solving a partial differential equation (PDE) allows for generalization from any 1D system to a 3D system, allowing for fungi growth to be applied to all manner of arbitrary geometries. This eliminates some computational difficulties with functional methods based on distance, as there is no ambiguity on overlapping nodes. Thus, this growth profile was modeled computationally as follows:

$$\frac{\partial \rho(x,t)}{\partial t} = D\nabla^2 \rho(x,t) \tag{1}$$

where the extent of the diffusion was tuned to experimental growth data and not allowed to reach full saturation. Here, ρ represents the local mycelial density, x the spatial position vector, t time, and D the effective diffusion coefficient. Two tests were used to calibrate

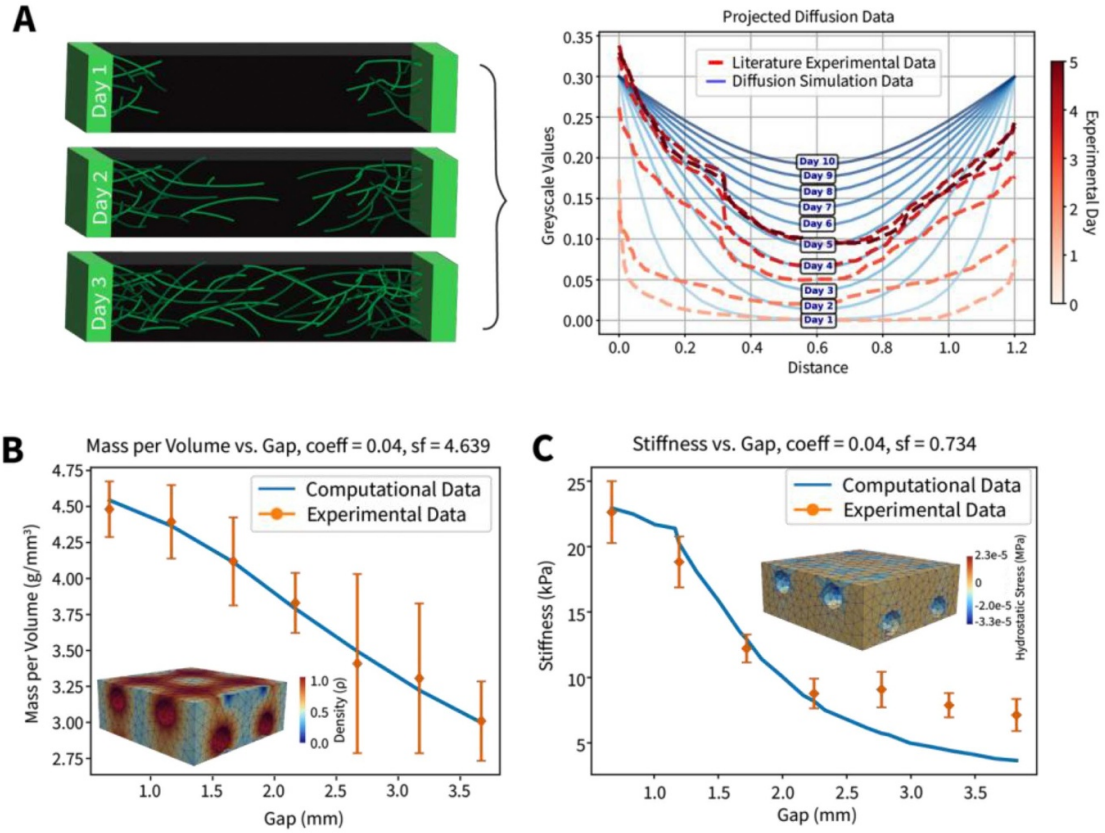

Figure 2. (A) A cartoon of confocal image grayscale values of fungi growth between two hydrogels, which were used to characterize the growth of fungi from a hydrogel substrate thanks to data from Gantenbein *et al* [18]. Diffusion front density values from solving equation (1) on a rectangular domain, overlaid on the calculated grayscale values of the confocal imaging. (B) Comparison of Gantenbein et al fungi biomass values vs simulation diffusion mass density as a function of print line gap. The computational density values were scaled linearly by a scaling coefficient of 4.639 with a diffusion coefficient of 0.04. (C) A similar comparison to literature values, in this case stiffness as a function of line gap. The computational stiffness values were scaled by a scaling factor of 0.734.

the model, 2D grayscale calibration and 3D biomass calibration.

In Gantenbein *et al*, two mycelium-inoculated hydrogel lines were tagged with fluorescent dye and placed between two rectangular slides [18]. The mycelium was allowed to grow for 5 d, where the density of fungal cells was quantified via laser confocal microscopy, giving insight to the relative density of fungal cells over time. For our model, we overlay the density profile over time from the literature against the density profile our model calculates in figure 2(B), giving us a starting point for tuning our diffusion coefficient and qualitatively validating our choice of a diffusion PDE to upscale into 3D.

To match the 1D grayscale tests, a rectangular grid was simulated with Dirichlet boundary conditions on the left and right side and zero flux at the top and bottom. Dirichlet boundary conditions of 0.3 were chosen to match the average grayscale values right at the edge of the hydrogel, when normalizing the image grayscale values between [0, 1] due to the uniformly fluorescent surface of the hydrogel having much higher grayscale values than even the densest parts of the fungal network immediately on the hydrogel surface. We enforce a 1D condition on our diffusion problem by setting no flux across the top and bottom boundary, allowing diffusion to occur only from one hydrogel face to another for a direct comparison with grayscale values. This setup served as a surrogate for the fungal growth profile observed in optical experiments. By comparing simulated fungal density distributions against the experimental grayscale data, as seen in figure 2(A), we gain qualitative insight into the correct shape of our growth model as well as a relative starting point for the diffusion coefficient scaling relative to the time step size. We then apply these insights to the 3D case of fungi growth from the surface of a hydrogel in a printed grid, albeit with direct quantitative scaling of the diffusion coefficient due to its sensitivity to time step and boundary conditions, allowing us to fully tune our biomass accumulation.

For the 3D biomass calibration, a full unit cell simulation was compared to empirical measurements of dry biomass as a function of print line gap for cuboids printed with uniformly spaced lines. Owing to the periodicity of the system, the diffusion equation was solved over only one of the

3D unit cells with the hydrogel surface as a fixed boundary of relative density $\rho_r(\partial\Omega, t) = 1$, with $\rho_r = \frac{\rho^*}{\rho_o}$, the ratio of the local density ρ^* to the maximum void density ρ_o. Periodic boundary conditions were applied t the x and y-plane sides as follows:

$$\begin{aligned}\rho_r(\mathbf{0}, t) - \rho_r(\boldsymbol{l},\ t) &= 0\\ \rho_r(\mathbf{0}, t) - \rho_r(\boldsymbol{w},\ t) &= 0\\ \rho_r(\mathbf{0}, t) - \rho_r(\boldsymbol{h},\ t) &= 0\end{aligned} \tag{2}$$

where the unit cell was bounded from 0 to l length, w width, and h height, and the boundary vectors as seen in figure 1(B):

$$\boldsymbol{l} = \begin{bmatrix} l \\ 0 \\ 0 \end{bmatrix},\ \boldsymbol{w} = \begin{bmatrix} 0 \\ w \\ 0 \end{bmatrix},\ \boldsymbol{h} = \begin{bmatrix} 0 \\ 0 \\ h \end{bmatrix}. \tag{3}$$

These periodic boundary conditions also served to correct for boundary effects, which are especially present at the sharp edges of the computational unit cell. Boundary conditions were enforced on two levels, the mesh-level and the solver-level. At the mesh level, periodic boundary conditions are set on all three axis face pairs (left/right, front/back, and bottom/top) using 4 × 4 affine translation matrices. Curve-level periodicity is pre-registered first to avoid seam-vertex matching failures on curved filament surfaces. At the solver-level, MOOSE's periodic boundary system automatically searches for matching nodes for primary and secondary boundary pairs via a translation vector. Biomass values were integrated across the domain and normalized by line spacing **g** to compute percent biomass, which was linearly scaled to fit experimental results. The diffusion coefficient was tuned by minimizing the root mean square error (RMSE) between simulation and experimental values via the Python library SciPy's optimization package. This minimization was solved using the Broyden–Fletcher–Goldfarb–Shanno algorithm, solving for

$$\min_{\rho>0} \epsilon = \sqrt{\sum_{i=1}^{n} \frac{(\widehat{\rho_i} - \rho_i)^2}{n}} \tag{4}$$

where $\widehat{\rho_i}$ are the literature biomass values for a given line spacing indexed at i, ρ_i are the simulated biomass values, and n are the number of literature observations. This tuning process resulted in an optimal diffusion coefficient of 0.04 $mm^2\ d^{-1}$ with the agreement of the biomass growth values demonstrated in figure 2(B). To empirically validate the relationship between print spacing and hyphal colonization predicted by our diffusion model, brightfield microscopy was used to visually confirm active mycelial bridging across the void spaces (see supplementary figure S2). This biological bridging directly corroborates the assignment of load-bearing capabilities to colonized regions within our FE model.

2.2. Linking biomass to structural stiffness

To relate mycelial density to mechanical properties, we drew from established models of cellular foams linking material properties to density [39]. These materials exhibit a power–law relationship as seen in the Gibson–Ashby model between density and stiffness of the form:

$$E = \alpha\rho^{\psi} \tag{5}$$

where E is the material stiffness, ρ the local mycelial density, α a linear scaling factor, and ψ an exponent describing the scaling behavior of the material.

Mechanically, the mycelium acts as a fibrous, percolating network in which load transfer occurs through the bending and stretching of interconnected hyphae. This structure bears conceptual similarity to open-cell foams and fiber-reinforced porous scaffolds, where mechanical performance depends primarily on the local density and connectivity of the network rather than the precise orientation of individual filaments. Directly modeling this architecture would require resolving thousands of branching filaments and their contact interactions, a computationally prohibitive task that is difficult to parameterize from experimental imaging data.

Therefore, the foam-based constitutive law provides a tractable mesoscale approximation that captures the dominant dependence of stiffness on biomass density. This formulation was implemented at the element level to assign spatially varying stiffness throughout the unit cell, consistent with the diffused fungal density field obtained in the previous step. Only the mycelium-filled regions were treated as structural, as the hydrogel matrix contributes negligible stiffness and is therefore numerically represented as voids [36].

To adapt the power scaling of stiffness seen in equation (5) to the nonlinear Yeoh hyperelastic model, we first start with the fundamental Yeoh strain energy density formulation:

$$W = \sum_{i=1}^{3} C_{i0}(\bar{I}_1 - 3)^i + \frac{K}{2}(J-1)^2 \tag{6}$$

where C_{i0} are empirically derived material constants, $\bar{I}_1$ is the first invariant of the isochoric right Cauchy–Green deformation tensor, K is the initial bulk modulus, and J is the elastic volume ratio. To map the material constants to relative density ρ_r, we define $C_{i0}(\rho_r)$ in the spirit of Gibson–Ashby as

$$C_{i0}(\rho_r) = C_{i0}^{\text{base}}(\rho_r)^{\psi}. \tag{7}$$

With C_{i0}^{base} defined as an empirical scaling factor. With a three-term model, C_{10} controls the linear regime of the curve, C_{20} controls the quadratic hardening of the material under compression, and C_{30} corresponds with cubic densification. To accurately represent the physical rigidity percolation threshold of the random fibrous network, a step-function cutoff was applied to the higher-order terms. Regions with a relative density below the critical connectivity threshold lack sufficient hyphal entanglement to undergo physical densification. Activating higher-order invariants in these highly compliant, fictitious void regions is known to induce severe numerical instability and artificial stiffening under large strains [39]. A connectivity threshold ρ_c of 0.01 was found to address numerical stability issues while adding negligible stiffness to our model. Thus, our localized parameters are defined as:

$$\begin{aligned} C_{10}(\rho_r) &= C_{10}^{\text{base}}(\rho_r)^{\psi} \\ C_{20}(\rho_r) &= \begin{cases} C_{20}^{\text{base}}(\rho_r)^{\psi} & \text{if } \rho_r \geqslant \rho_c \\ 0 & \text{if } \rho_r < \rho_c \end{cases} \\ C_{30}(\rho_r) &= \begin{cases} C_{30}^{\text{base}}(\rho_r)^{\psi} & \text{if } \rho_r \geqslant \rho_c \\ 0 & \text{if } \rho_r < \rho_c \end{cases} \end{aligned} \quad . \tag{8}$$

To vary bulk modulus by elemental stiffness, we start with the relationship between bulk modulus K, initial shear modulus μ, and Poisson's ratio ν:

$$K = \frac{2\mu(1+\nu)}{3(1-2\nu)}. \tag{9}$$

The consistency condition for the Yeoh model defines $\mu = 2C_{10}(\rho_r)$. Assuming a Poisson's ratio of 0.1, consistent with open-cell biological foams [40], we simplify the relationship between K and ρ_r as:

$$K(\rho_r) = C_{10}(\rho_r)\left[\frac{4(1+\nu)}{3(1-2\nu)}\right] \approx 1.833 C_{10}(\rho_r). \tag{10}$$

This allows us to maintain the physical compressibility of an open-cell foam regardless of fungal density.

Uniaxial compression simulations were performed by assigning the top boundary of the unit cell a constant displacement of $0.01t$ (mm s^{-1}), then fixing the z displacement of the bottom face. A single bottom node is also pinned in the x and y direction to eliminate rigid-body motion without overconstraining shear. Finally, periodic displacement conditions were assigned to the opposite side faces. Additionally, a frictionless contact penalty of 10^6 was applied to the hydrogel surface. Through this study, we aim to recreate the relationship between line gap and 25% compressive strain stiffness Gantenbein *et al* used as a benchmark for comparing the relative strength of spaced hydrogels [18]. Instantaneous stiffness was measured for computational samples by calculating the slope of the secant line for datapoints immediately before and after the 25% strain target. In effect, we are homogenizing the local elemental stiffness to the macroscopic stiffness of the entire unit cell, which is then calibrated experimentally. Coefficients ψ, C_{10}, C_{20}, C_{30} and a numerical fitting parameter β were optimized by minimizing, in the same manner as the diffusion values, the RMSE between simulation predictions and mechanical test results at the end-of-growth stage for physical samples, demonstrated in figure 2(C). This resulted in a linear scaling coefficient $\alpha = 0.744$, $C_{10} = 1\text{e}^{-09}$, $C_{20} = 1.5\text{e}^{-07}$, $C_{30} = 2\text{e}^{-07}$, and an exponential factor $\psi = 8$ at a mean RMSE of 1.3845 kPa. While the scaling α value represents the relative intrinsic modulus of a fully dense, completely saturated mycelial volume and likely accounts for errors in the diffusive density values, the low C_{i0} values correspond with the unit scaling of empirical materials at the low kPa stiffness range for a model designed around loads on the scale of MPa. Furthermore, the greater contribution of C_{20} and C_{30} is attributed to the extremely soft, non-linear nature of the material even at initial loading.

While classical Gibson–Ashby open-cell foams typically exhibit a density-stiffness exponent near $\psi = 2$, our hyperelastic calibration required a much larger exponent. This deviation is physically consistent with the mechanics of highly irregular, random networks, such as aerogels, which routinely exhibit scaling exponents well above classical bounds due to incomplete connectivity and the presence of non-load-bearing 'dangling' structures [39]. The macroscopic stiffness of fibrous networks is likely governed by a rigidity percolation threshold: load transfer only occurs once a critical biological density is achieved, as the presence of mycelium fibers does not guarantee they are dense enough to interlock. Because the phenomenological power–law implemented in our model from equation (5) does not explicitly subtract this critical threshold, the apparent scaling exponent (ψ) must naturally inflate. The high exponent acts as a mathematical surrogate for rigidity percolation, correctly driving the mechanical contribution of sub-critical, unbridged diffused densities to near zero [41].

The close alignment between the computational predictions and experimental outcomes, particularly regarding fungal growth modeled via diffusive front, suggests that the macroscale behavior of mycelial colonization and overall biomass generation can be effectively approximated using a simple and computationally inexpensive partial differential equation. These findings indicate that fungal biomass accumulation over time can be accurately modeled without the need for detailed and complex, resource-intensive microscale simulations. This serves to greatly simplify

predictive calculations related to growth rate and material deposition with minimal parametrization.

However, modeling the mechanical response under compression presents more challenges. While the diffusion-based model provides a reasonable approximation of biomass distribution, it does not capture the morphological complexity of fungal growth. Fungal mycelia exhibit a fibrous, branching architecture that is highly hierarchical, with microscale entanglement and orientation influencing macroscale mechanical properties. The isotropic and scalar nature of the diffusion model overlooks these directional and structural nuances, which may limit its effectiveness in predicting stiffness or failure modes in real-world applications despite the model's strong applicability for this case. For the purposes of this study, these limitations are not applicable and are only raised for future studies.

Together, these calibrated parameters form a consistent link between biological growth, spatially resolved material distribution, and macroscopic mechanical performance. This calibrated model provides a foundation for topology optimization efforts via a scaled computational framework, allowing us to explore strength-to-weight tradeoffs across a discrete design space of printable geometries.

3. Optimization of printed structures

To optimize the structural efficiency of the mycelium-based hydrogel structures, we employed a Bayesian optimization framework using the BoTorch package [42] which is a Python library built on Gaussian process (GP) modeling. This method is particularly well-suited for optimization problems with low-dimensional, expensive-to-evaluate design spaces, which is particularly relevant for the constrained unit cell topology problem defined here.

Thanks to the reduced complexity of the unit cell design space characterized by just two primary geometric parameters $x = (g, h)$ with g (line gap) and h (overhang), normalized to a rescaled domain of $\Omega = [0, 1]^2$, the typically intensive task of topology optimization becomes much more computationally tractable. Bayesian optimization iteratively explores this space by modeling the objective functions with a GP, then using an acquisition function to balance exploitation of known optima with exploration of uncertain regions. For our study, the expected improvement (EI) acquisition function was chosen to guide the optimization, with the schematic of the process illustrated in figure 1(C).

Restricting the design space of the topology optimization problem to a unit-cell-based design space significantly improves the computational efficiency of our problem. Bayesian optimization, when applied to this discretized space, enabled rapid identification of optimal design configurations without the need for full-field FE simulations. This approach is especially useful in exploratory phases or when varying critical material parameters, such as ink composition or initial fungal density. The reduced computational burden opens the possibility for iterative prototyping and real-time feedback in future smart manufacturing pipelines.

The optimization framework targets two related but distinct objectives: maximizing the specific stiffness and minimizing the mass for a target stiffness. These objectives were selected to balance mechanical performance and material efficiency, reflecting the core engineering trade-off underlying sustainable additive manufacturing. High specific stiffness is a critical property for lightweight structural components, particularly in aerospace and architectural applications, where maximizing load-bearing capacity while minimizing material usage directly translates to reduced environmental impact and improved structural efficiency. Conversely, minimizing mass for a given stiffness provides insight into the material distribution strategies that achieve equivalent performance with lower resource consumption. Both targets represent design objectives consistent with those of the larger aerospace industry.

3.1. Maximizing specific stiffness

Defined as the ratio of unit cell stiffness $E(x)$ to the total mass $M(x)$ of the unit cell, the specific stiffness γ is a common metric for mechanical material efficiency. This optimization objective can be represented as

$$\max_{0<\rho} \gamma = \frac{E(x)}{\rho_{\text{unit cell}}}, \tag{11}$$

where the unit cell density is derived from the total mass of hydrogel and fungi within the unit cell volume $V_{\text{unit cell}}$,

$$\rho_{\text{unit cell}} = \frac{M_{\text{fungi}}(x) + M_{\text{hydrogel}}(x)}{V_{\text{unit cell}}}. \tag{12}$$

Given empirical evidence showing that mycelial biomass constitutes only ~4% of the total mass of the structure [18], we assume $m_{\text{fungi}} \ll m_{\text{hydrogel}}$. Under this approximation, the optimization function simplifies to:

$$\max_{0<\rho} \gamma = \frac{E(x)\, V_{\text{unit cell}}}{M_{\text{hydrogel}}(x)}. \tag{13}$$

3.2. Minimizing mass for a target stiffness

A second optimization condition seeks to minimize the mass of the printed structure while maintaining a target range of stiffness values. In this formulation, the objective becomes:

$$\min_{0<\rho} M(x) = \int_0^{\Omega} \rho \, \mathrm{d}\Omega. \tag{14}$$

A conditional constraint was applied to the optimization loop to restrict valid solutions to those achieving a specified stiffness tolerance. This conditional optimization was achieved following the framework described in the work of Eriksson and Poloczek [43] regarding scalable constrained Bayesian optimization. To design our optimization, equation (14) was subjected to the constraints $c_1(x)$ and $c_2(x)$

$$\begin{aligned} E_{\min} \leqslant E(x) \leqslant E_{\max} \\ c_1(x) = E_{\min} - E(x) \leqslant 0. \\ c_2(x) = E(x) - E_{\max} \leqslant 0 \end{aligned} \tag{15}$$

In each Bayesian optimization iteration, three GP models are fitted: GP_f for the objective function $f(x)$, GP_{c1} for the lower-bound stiffness constraint, and GP_{c2} for the upper-bound stiffness constraint, assuming independent priors and posteriors across outputs. All GPs follow an ARD RBF kernel. Although we may see some uncertainty at the areas of step discontinuities for unit cells, this is a product of our pragmatic choice to enforce whole unit cells. The hyperparameters for our kernels were fit by maximizing the marginal log likelihood (MLL), using the L-BFGS-B minimization scheme. The fitting of hyperparameters was performed after every Bayesian optimization loop, where they were optimized by maximizing the sum of the individual MLLs. Our optimization loop started with 20 initial samples.

Like with standard Bayesian Optimization, our constrained optimization model chooses sampling points via an acquisition function trading off exploitation and exploration. In our case, we use q-Log EI, a variant of the standard EI acquisition function that computes a batched smoothed log-improvement over the function. For the constrained EI objective, the objective $\alpha(X)$ for data X is defined as

$$\alpha_\eta(X) \sim= \mathbb{E}\left[\mathrm{Imp}\left(f(X);f^*\right) \cdot \prod_{j=1}^{J} \sigma\left(-\frac{c_j(X)}{\eta}\right)\right] \tag{16}$$

where η is a sigmoid sharpness parameter, $f(x)$ is the new measured value, and $f^*(x)$ is the known best value. This formulation penalizes the improvement $\mathrm{Imp}\left(f(X);f^*\right)$ by the weighted product of the constraint functions, seen in $\prod_{j=1}^{J} \sigma\left(-\frac{c_j(X)}{\eta}\right)$. If $c \ll 0$ (the point is considered strongly feasible by the constraints), the point is likely to be chosen. In our design, for each loop 512 samples were assessed before a new sample was simulated. To maximize the EI, SciPy's L-BFGS-B optimizer was used, with 20 restarts from 1024 Sobol samples.

In both cases, a maximum of 1000 iterations were run per optimization campaign with an additional stopping criterion of 0.5% relative improvement over a 50-iteration window. These experiments were performed in triplicate, with convergence being achieved before the 50 iterations threshold.

For the specific stiffness optimization scheme, the resulting specific stiffness values exhibited maxima at parameter combinations of $g = 0.81$ and $h = 0.56$, aligning closely with the trends observed in experimental testing from previous literature [18]. These findings support the consistency of the simulation framework in capturing biologically driven material behavior, and are visualized in figures 3(A)–(D), demonstrating the full pathway of the minimization of the specific stiffness of the material.

Because the density of the material directly influences the specific stiffness outcome, the print density was fixed according to experimentally validated values for the hydrogel formulation. This constraint ensures the results remain physically realizable within the tested fabrication process.

When the optimization objective was shifted toward minimizing mass while achieving a target stiffness, multiple viable topologies emerged, as seen in figure 3(C). Among these, specific designs with reduced hydrogel usage were identified as optimal through the same Bayesian framework. As expected, a general inverse correlation was observed between print mass and print spacing. Larger values of g and h reduced the quantity of hydrogel required, thereby decreasing the overall mass of the structure. This trend is consistent with the hydrogel being the dominant contributor to mass, given that mycelial dry biomass accounts for only a small fraction ($\sim$4%) of total print weight.

However, due to the parametric nature of the unit cell approach and the constraint of full-cell tessellation to fill a 25 mm cubic print volume, the final print mass field displayed a jagged response surface. This effect was especially pronounced for smaller unit cells, where variations in integer tessellation count introduced abrupt shifts in total material volume. The inability to use fractional unit cells led to slight oversizing or under sizing relative to the target print dimensions, producing local discontinuities in the mass optimization surface.

Through the compression simulations, a clear global trend emerged: as both spacing parameters g and h increased, total print mass decreased. Meanwhile, the optimal specific stiffness was found near intermediate values around $g = 0.81$ mm and $h = 0.56$ mm suggesting a balance between structural efficiency and material conservation in the selected designs at least within a relatively limited design window.

Analysis of the optimization results reveals that the highest compressive stiffness corresponds to designs with relatively small gaps between hydrogel

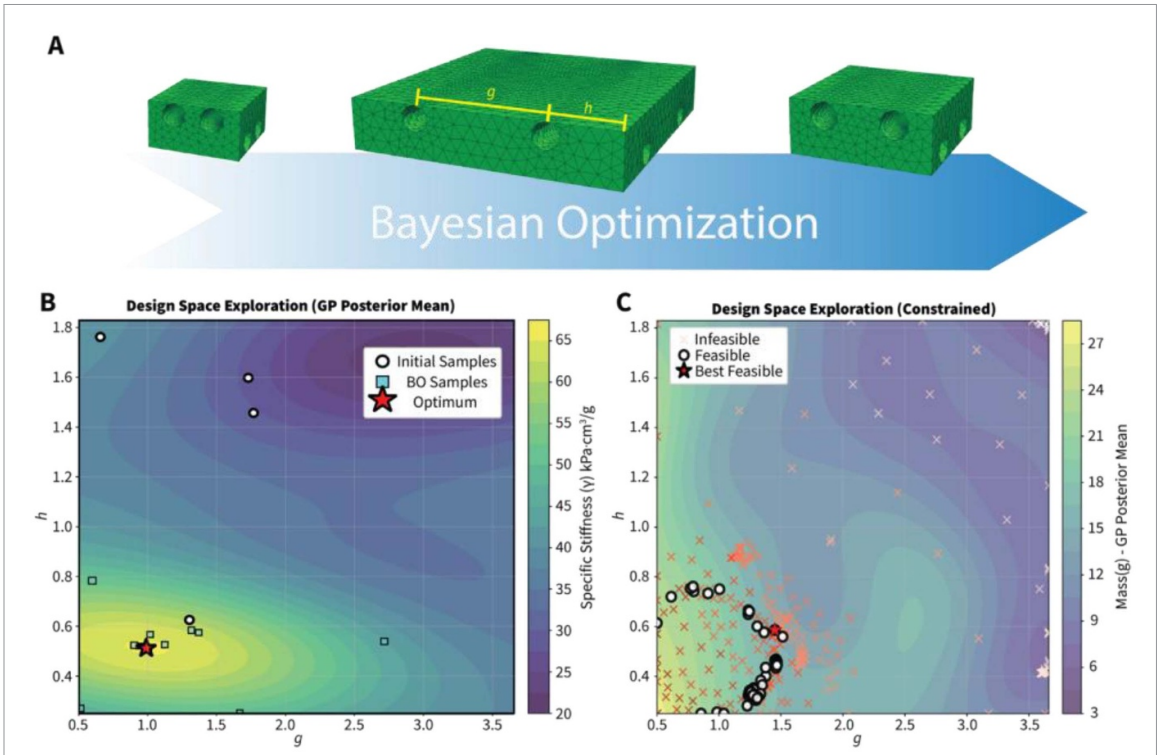

Figure 3. (A) Representation of changing unit cell designs through Bayesian optimization. (B) Posterior mean of the Bayesian optimization search space for the maximum specific stiffness, maximizing the specific stiffness target. (C) Bayesian optimization search space for the constrained optimization of mass (for a targeted stiffness value). In this case, mass was minimized in order to find a specific stiffness within the 19–18.5 kPa range.

print lines. Designs with excessively sparse line spacing lacked sufficient hydrogel substrate for effective mycelial scaffold formation, resulting in weaker mechanical performance despite a reduction in mass. Conversely, denser prints allowed for more complete mycelial colonization and stronger lattice structures but incurred a higher material cost. In addition, too small a line gap does not provide enough of a void for the fungi to grow into, reducing cementation. The topology optimization framework consistently favored slightly denser structures, demonstrating a tradeoff in which modest increases in material usage yield substantial gains in stiffness and reliability.

This insight reveals a fundamental challenge in the application of 3D-printed fungal materials: mycelial scaffolds require a significant volume of hydrogel to develop structural integrity. Although post-processing techniques such as freeze-drying can be used to remove excess hydrogel and reduce final weight while maintaining form, such methods also kill the living fungus, negating one of the core advantages of ELMs, namely, self-healing and environmental adaptivity [44].

Despite the simplifications inherent in the model, the unit cell approach proved to be a computationally efficient and physically consistent strategy for approximating structural behavior under uniaxial compression. The method provided accurate results for normal loading conditions and enabled efficient exploration of the design space. However, the same unit cell simplification is unlikely to hold for bending or torsional loading scenarios, where the force distribution would interact with more anisotropic microstructural features.

4. Experimental verification and mechanical testing

To validate the optimized topologies, we fabricated and tested physical samples using a direct ink writing (DIW) bioprinting process. The mycelium hydrogel ink was prepared using a formulation modeled after that reported by Gantenbein *et al* [18].

4.1. Materials

The following chemicals were purchased and used as received: Gibco™ Bacto Malt Extract (Fisher Scientific), peptone (Merck Sigma), calcium chloride anhydrous (Merck Sigma), sodium alginate (Merck Sigma), agar–agar (Carl Roth), and κ-Carrageenan (Merck Sigma). A cellulose-based thickener (MCG, Vivapur MCG 811 P) was provided by JRS Pharma. The fungal species *Ganoderma lucidum* (strain number M9726) was purchased from Mycelia NV.

4.2. Mycelium cultivation

Mycelium for bioinks is prepared in a two-stage process. The fungus is grown on malt extract agar (MEA)

plates to prevent and visually assess for contamination throughout the experiment. MEA plates were inoculated, incubated at 27 °C for 7 d, and stored at 4 °C for up to 21 d. Two rectangles (5 mm x 10 mm) are cut from the MEA and added to a sterile Erlenmeyer flask with a cotton stopper containing 150 mL of malt extract broth. The flask is vigorously shaken to loosen the hyphal tips and incubated for 7 d at 27 °C, shaken at 160 rpm. The 'seed' inoculum is washed three times from the broth into 25 mL of sterile DI water in 50 ml Falcon tubes. The pellets are vortexed for one minute to break them into smaller hyphal fragments for reseeding, and they are stored at 4 °C up to 21 d.

4.3. Mycelium bioink preparation

Mycelium-inoculated bioinks were formulated in DI water containing 10 wt% malt extract, 0.5 wt% peptone, 3.0 wt% cellulose-based thickener, 1.5 wt% κ-carrageenan, and 1.5 wt% agar, following [18]. The malt extract and peptone were dispersed into DI water, mixed with a liquid frother attached to a hand rotary tool (Proxxon, No 28 505–11) at 5,000 rpm for 30 s, and heated to ∼60 °C. The cellulose-based thickener was added and mixed for 30 s, and allowed to rest for 10 min to allow the cellulose to swell. The remaining additives were mixed individually for 30 s, yielding a paste-like mixture. The bioink was sterilized via autoclave (Hirayama HG-50), at 121 °C for 20 min. As the ink cooled from 50 °C to room temperature, it was mixed for 30–60 s every 5 min under sterile conditions in a biosafety cabinet (Herasafe). This step forms microgranules during agar setting, which are important for the rheology of the DIW bioink. Seed mycelium grown in liquid culture was harvested as outlined above, and 1 ml of fragments (for every 50 ml of ink) was mixed into the bioink. Roughly 20 ml of bioink was added to 20 ml syringes and degassed via centrifugation at 1690 g for one minute. The bioink was typically used immediately for DIW or stored, sealed at 4 °C, when not in use, to inhibit mycelium growth before printing.

4.4. DIW

DIW in this work was prepared on a modified Ultimaker 2+ desktop 3D printer as described in Amani *et al* [45]. Designed patterns were prepared via fullcontrol, with printing and travel speeds set to 15 and 30 mm s^{-1}, respectively, and a layer height of 0.84 mm for a nozzle diameter of 0.84 mm. The prints were incubated in sterile boxes at 27 °C for 15 d. Five distinct print topologies were selected for empirical testing, covering both the bounds of the design space and the predicted optima from Bayesian optimization ($g = 0.66$, $h = 0.33$; $g = 3.66$, $h = 1.83$; $g = 3.66$, $h = 0.33$), as well as the full field design optimum and a midpoint design at $g = 1.23$, $h = 0.68$. These topologies varied in their g and h parameters. Each design was printed in triplicate. Because our computational framework optimizes for the terminal, fully colonized state of the material, mechanical testing was focused exclusively on this 15 d end-point. Macroscopic time-course imaging of the grid structures (supplementary figure S1) illustrates the temporal evolution of the fungal network, visually confirming that bulk colonization plateaus after this period of incubation. To ensure that the observed structural integrity was driven by mycelial biomass accumulation rather than hydrogel desiccation or shrinkage, all physical samples were incubated in a controlled environment at ∼80% relative humidity.

4.5. Mechanical testing

After incubation, samples were weighed to calculate their specific stiffness values. Mechanical properties were evaluated via compression testing using a Zwick Roell UTS with a 100 N load cell at a constant displacement rate of 5 mm min^{-1} as seen in the configuration shown in figure 1(d). Each sample was compressed at a constant displacement rate of 5 mm min^{-1} [46]. Compressive stiffness was quantified by calculating the slope of the force-displacement curve between 24% and 26% strain, following the instantaneous stiffness calibration values from Gantenbein *et al* [18]. The experimental testing confirmed the validity of the computational optimization framework. Specifically, the topology configurations predicted to yield maximum specific stiffness were successfully replicated in physical prints. Each of the five candidate designs (three from the borders of the design space and two from the optimization-predicted optima) was fabricated and tested in triplicate, as seen in figure 4(A). These specimens displayed a hyperelastic material response typical of soft matter biological materials, as seen in figure 4(B). When testing the extrema print designs ($g = 0.66$ and $h = 0.33$, $g = 3.66$ and $h = 1.83$) against the optimal print design ($g = 0.81$, $h = 0.56$), we find that this print has a consistently higher stiffness through the entire loading path.

Mechanical testing results aligned closely with simulation predictions, with simulated stress values for each design falling within the calibration range used during model development, shown in figure 4(C). This agreement validates both the fungal growth model and the material property scaling functions employed in the FE simulations, though it is important to acknowledge inter-strain variability will likely require re-calibration for mechanical data. Even within species, mycelium have shown differences in growth kinetics under equivalent conditions [44].

Consistently, the simulation agreement with the experimental curves both in the literature and in our tests tended to diverge past the 30% strain point,

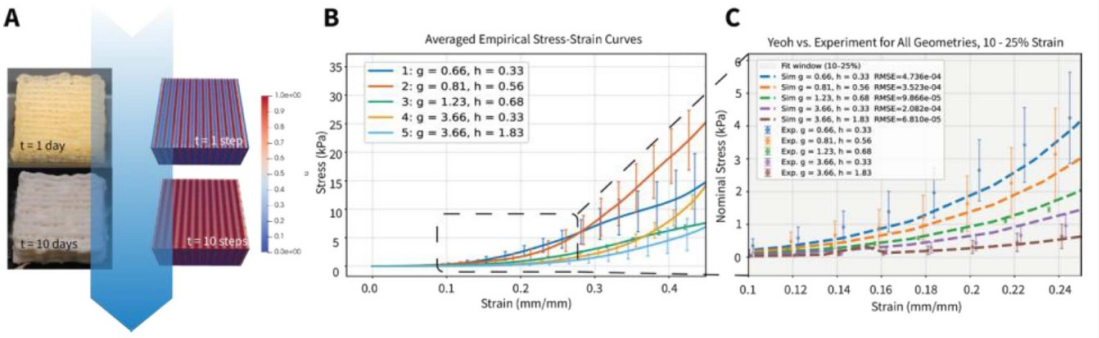

Figure 4. (A) Time-based comparison of a printed fungi grid with the computational diffusion model. (B) Empirical stress–strain curves for printed cuboids. Designs were printed in triplicate and averaged with error bars shown. (C) Comparison of the Yeoh hyperelastic model against experimental data within the 10%–25% strain range.

and also in designs with rather large line gaps, such as those past 2.25 mm. This is likely due to our decision to omit the modeling of the soft hydrogel within the mycelium matrix. Past 30% strain, the fungi has completely compressed, and the hydrogel begins to significantly buckle and then burst, as noted in Gantenbein *et al* [18]. The additional compliance of the hydrogel structure likely causes an under-stiffening of the material, offsetting the exponential densification modeled in the Yeoh model. On the other end, at low strains, there is a consistent divergence at large line gaps, as seen in figure 2(C). Partially, this is due to the mycelium not sufficiently colonizing large gaps to reach the stiffness percolation threshold, as seen in supplementary figure S2, where the only measurable stiffness is in the hydrogel compacting itself. This also explains why the stiffness noticeably plateaus past this point. The hydrogel also visibly slumps at larger line gaps, as in supplementary figure S5, indicating buckling or filament bending is the real failure mode at these designs, well before fungi compression and densification can occur.

5. Conclusions

We develop a FE-based computational framework to approximate the growth behavior and mechanical performance of 3D-printed mycelium hydrogel structures. Leveraging this model, we implemented a hierarchical topology optimization scheme that couples fungal growth dynamics with structural performance prediction, enabling data-driven optimization of bio-fabricated geometries. This represents one of the first demonstrations of integrating a living growth model within an optimization framework traditionally reserved for synthetic materials.

Our results demonstrate that diffusion-based models serve as effective macroscale approximations for mycelial growth, providing quantitatively reliable estimates of biomass distribution and corresponding stiffness evolution. Through this coupling, we revealed how biological growth parameters and geometric design interact hierarchically: from microscale hyphal diffusion to macroscale structural response. Notably, the optimization yielded non-intuitive design configurations in which moderate filament spacing produced superior specific stiffness, underscoring the importance of considering both biological and structural factors in tandem. It is important to note that fungal growth kinetics are highly organism and strain-specific. The phenomenological scaling parameters D, α, ψ, developed in this study are not universal constants, but rather strain-specific inputs. By utilizing standard physical growth characterizations, this calibration-to-simulation framework can be readily adapted to other fungal species or strains, enhancing its generalizability as a design tool for diverse ELMs.

Beyond the immediate computational insights, this work highlights the potential of hierarchical design principles for the next generation of ELMs. By linking the self-organizing properties of biological systems with formal optimization methods, we establish a new paradigm for biohybrid material design: one where growth and geometry co-evolve toward structural efficiency.

While the diffusion-based formulation simplifies the morphogenetic complexity of mycelium networks, the present framework demonstrates that even reduced-order biological models can successfully guide functional design at larger scales. Future developments should extend this approach to more complex loading regimes (e.g. bending, torsion, cyclic loading) and incorporate true multiscale constitutive models to capture the anisotropic mechanics of fibrous fungal networks.

Ultimately, this study advances the field by showing that hierarchical topology optimization can serve as a bridge between living biological growth and computational material design; transforming 3D-printed

fungal hydrogels from proof-of-concept biomaterials into systematically engineered, high-performance structures.

Acknowledgments

This research was carried out under project number T24003 in the framework of the Research Program of the Materials innovation institute (M2i) (www.m2i.nl) and was funded by Holland High Tech | TKI HTSM via the PPS allowance scheme for public-private partnerships.

This research also received support from the Delft Institute for Computational Science and Engineering (DCSE), using resources from the Technische Universiteit Delft DelftBlue high performance computer.

Data availability statement

The data that support the findings of this study are available from the corresponding author upon reasonable request, and supplementary data for experimental stress strain curves are attached. Source codes for meshing, topology optimization, and finite element simulations is available through our GitLab page https://gitlab.tudelft.nl/shapingmatterlab.

Raw Compression Data available at http://doi.org/10.1088/1758-5090/ae7835/data1.

Supplementary Figures and Information available at http://doi.org/10.1088/1758-5090/ae7835/data2.

Conflict of interest

The authors declare that they have no known competing financial interests or personal relationships that could have appeared to influence the work reported in this paper.

Author contributions

Winston Lindqwister 0000-0002-1657-5701
Conceptualization (lead), Data curation (equal), Formal analysis (lead), Investigation (lead), Methodology (lead), Project administration (equal), Software (lead), Validation (lead), Visualization (lead), Writing – original draft (lead), Writing – review & editing (lead)

Mrinal Chaudhury 0009-0006-6714-4561
Data curation (supporting), Investigation (supporting), Methodology (supporting), Validation (supporting), Writing – review & editing (supporting)

Sarah Schyck 0000-0002-9731-2160
Formal analysis (supporting), Investigation (supporting), Methodology (supporting), Validation (supporting)

Iuri Rocha 0000-0001-8410-3741
Conceptualization (supporting), Funding acquisition (equal), Project administration (equal), Supervision (equal), Writing – review & editing (equal)

Kunal Masania 0000-0001-9498-1505
Conceptualization (equal), Data curation (equal), Funding acquisition (equal), Methodology (supporting), Project administration (equal), Resources (equal), Supervision (equal), Writing – review & editing (equal)

Martin Lesueur 0000-0001-9535-2268
Conceptualization (equal), Data curation (equal), Formal analysis (supporting), Funding acquisition (equal), Investigation (supporting), Methodology (equal), Project administration (equal), Supervision (equal), Writing – review & editing (equal)

References

[1] An B, Wang Y, Huang Y, Wang X, Liu Y, Xun D and Church G M 2023 Engineered living materials for sustainability *Chem. Rev.* **123** 2349–419
[2] Wang Q, Hu Z, Li Z, Liu T and Bian G 2023 Exploring the application and prospects of synthetic biology in engineered living materials *Adv. Mater.* **37** e2305828
[3] Heveran C M, Williams S L, Qiu J, Artier J, Hubler M H, Cook S M, Cameron J C and Srubar W V III. 2020 Biomineralization and successive regeneration of engineered living building materials *Matter* **2** 481–94
[4] Nettersheim I H M S, Sotelo N S G, Verdonk J C and Masania K 2024 Engineered living composite materials *Compos. Sci. Technol.* **256** 110758
[5] Rodrigo-navarro A, Sankaran S, Dalby M J, Del Campo A and Salmeron-sanchez M 2021 Engineered living biomaterials *Nat. Rev. Mater.* **6** 1175–90
[6] Srubar W V III 2021 Engineered living materials: taxonomies and emerging trends *Trends Biotechnol.* **39** 574–83
[7] Molinari S, Tesoriero R F Jr and Ajo-franklin C M 2021 Bottom-up approaches to engineered living materials: challenges and future directions *Matter* **4** 3095–120
[8] Pahuja P 2025 Engineered living materials based on fungi *Fungal Biotechnology* (Elsevier) pp 133–59
[9] Li K, Wei Z, Jia J, Qing X, Liu H, Zhong C and Huang H 2023 Engineered living materials grown from programmable Aspergillus niger mycelial pellets *Mater. Today Bio.* **19** 100545
[10] McBee R M *et al* 2022 Engineering living and regenerative fungal-bacterial biocomposite structures *Nat. Mater.* **21** 471–8
[11] Olsson S and Hansson B S 1995 Action potential-like activity found in fungal mycelia is sensitive to stimulation *Sci. Nat.* **82** 30–31

[12] Beasley A E, Tsompanas M-A and Adamatzky A 2023 Fungal photosensors *Emergence, Complexity and Computation* (Springer) pp 123–30
[13] Khalid M Y, Arif Z U, Tariq A, Hossain M, Umer R and Bodaghi M 2024 3D printing of active mechanical metamaterials: a critical review *Mater. Des.* **246** 113305
[14] Coasne B 2016 Multiscale adsorption and transport in hierarchical porous materials *New J. Chem.* **40** 4078–94
[15] Hartmann M and Schwieger W 2016 Hierarchically-structured porous materials: from basic understanding to applications *Chem. Soc. Rev.* **45** 3311–2
[16] Parlett C M A, Wilson K and Lee A F 2013 Hierarchical porous materials: catalytic applications *Chem. Soc. Rev.* **42** 3876–93
[17] Jones J R, Lee P D and Hench L L 2006 Hierarchical porous materials for tissue engineering *Phil. Trans. A Math. Phys. Eng. Sci.* **364** 263–81
[18] Gantenbein S, Colucci E, Käch J, Trachsel E, Coulter F B, Rühs P A, Masania K and Studart A R 2023 Three-dimensional printing of mycelium hydrogels into living complex materials *Nat. Mater.* **22** 128–34
[19] Gandia A and Adamatzky A 2024 Fungal skin for robots *BioSystems* **235** 105106
[20] Olivero E *et al* 2023 Gradient porous structures of mycelium: a quantitative structure-mechanical property analysis *Sci. Rep.* **13** 19285
[21] Schyck S, Marchese P, Amani M, Ablonczy M, Spoelstra L, Jones M, Bathaei Y, Bismarck A and Masania K 2024 Harnessing fungi signaling in living composites *Glob. Chall.* **8** 2400104
[22] Nopharatana M, Howes T and Mitchell D 1998 Modelling fungal growth on surfaces *Biotechnol. Tech.* **12** 313–8
[23] Chertov O, Gorbushina A and Deventer B 2004 A model for microcolonial fungi growth on rock surfaces *Ecol. Modell.* **177** 415–26
[24] Naboni R, Kunic A and Breseghello L 2020 Computational design, engineering and manufacturing of a material-efficient 3D printed lattice structure *Int. J. Archit. Comput.* **18** 404–23
[25] Lu L, Sharf A, Zhao H, Wei Y, Fan Q, Chen X, Savoye Y, Tu C, Cohen-or D and Chen B 2014 Build-to-last: strength to weight 3D printed objects *ACM Trans. Graph.* **33** 1–10
[26] Zhu J-H, Zhang W-H and Xia L 2016 Topology optimization in aircraft and aerospace structures design *Arch. Comput. Methods Eng.* **23** 595–622
[27] Keane A J and Scanlan J P 2007 Design search and optimization in aerospace engineering *Phil. Trans. A Math. Phys. Eng. Sci.* **365** 2501–29
[28] Wang L, Du W, Pengfei H and Yang M 2020 Topology optimization and 3D printing of three-branch joints in treelike structures *J. Struct. Eng.* **146** 04019167
[29] Groen J P and Sigmund O 2018 Homogenization-based topology optimization for high-resolution manufacturable microstructures *Int. J. Numer. Methods. Eng.* **113** 1148–63
[30] Vantyghem G, De Corte W, Shakour E and Amir O 2020 3D printing of a post-tensioned concrete girder designed by topology optimization *Autom. Constr.* **112** 103084
[31] Xie L, Zhang Y, Minghui G and Zhao Y 2022 Topology optimization of heat sink based on variable density method *Energy Rep.* **8** 718–26
[32] Tran Q D, Shin D and Jang G-W 2024 Bayesian optimization-based topology optimization using moving morphable bars for flexible structure design problems *Eng. Struct.* **300** 117103
[33] Sattari K, Yuchao W, Chen Z, Mahjoubnia A, Changhua S and Lin J 2024 Physics-constrained multi-objective Bayesian optimization to accelerate 3D printing of thermoplastics *Addit. Manuf.* **86** 104204
[34] Luong P, Gupta S, Nguyen D, Rana S and Venkatesh S 2019 Bayesian optimization with discrete variables *AI 2019: Advances in Artificial Intelligence (Lecture Notes in Computer Science)* (Springer) pp 473–84
[35] Geuzaine C and Remacle J-F 2009 Gmsh: a 3-D finite element mesh generator with built-in pre- and post-processing facilities: the Gmsh paper *Int. J. Numer. Methods Eng.* **79** 1309–31
[36] Harbour L *et al* 2025 4.0 MOOSE: enabling massively parallel multiphysics simulation *Software X* **31** 102264
[37] Du H, Tran T-B-T and Perré P 2019 A 3-variable PDE model for predicting fungal growth derived from microscopic mechanisms *J. Theor. Biol.* **470** 90–100
[38] Boswell G P and Davidson F A 2012 Modelling hyphal networks *Fungal Biol. Rev.* **26** 30–38
[39] Broedersz C P and MacKintosh F C 2014 Modeling semiflexible polymer networks *Rev. Mod. Phys.* **86** 995–1036
[40] Chen H, Schmidt B, Gennett A, Kamm P H, Gurlo A, Meyer V and Simon U 2025 Extrusion-based additive manufacturing of complex three-dimensional ultra-lightweight materials using the basidiomycete Fomes fomentarius *Mater. Adv.* **6** 5149–58
[41] Aney S, Pandit P, Ratke L, Milow B and Rege A 2025 On the origin of power-scaling exponents in silica aerogels *J. Sol-Gel Sci. Technol.* **114** 98–105
[42] Balandat M, Karrer B, Jiang D R, Daulton S, Letham B, Wilson A G and Bakshy E 2020 BoTorch: a framework for efficient Monte-Carlo Bayesian optimization *Advances in Neural Information Processing Systems* vol 33 (arXiv: 1910.06403)
[43] Eriksson D and Poloczek M 2021 Scalable constrained Bayesian optimization *Int. Conf. on Artificial Intelligence and Statistics* pp 730–8
[44] Elsacker E, Zhang M and Dade-robertson M 2023 Fungal engineered living materials: the viability of pure mycelium materials with self-healing functionalities *Adv. Funct. Mater.* **33** 2301875
[45] Amani M, Weiland K, Ablonczy M, Guevara-sotelo N S, Zygouris I, van Stuyvesant Meijen J and Masania K 2026 Enhancing the ultrasonic welding of wood using 3D printed lignin energy directors *Adv. Sci.* **13** e07055
[46] Kimura Y, Kato K and Matsuda A 2019 Study on voxel finite element analysis of open-cell polyurethane foam *IOP Conf. Ser. Mater. Sci. Eng.* **548** 012010